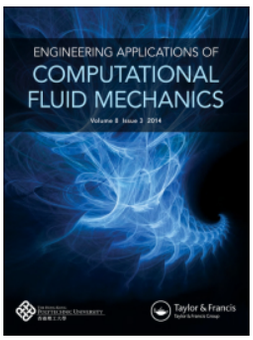

Engineering Applications of Computational Fluid Mechanics

ISSN: (Print) (Online) Journal homepage: https://www.tandfonline.com/loi/tcfm20

Influence of wind barrier on the transient aerodynamic performance of high-speed trains under crosswinds at tunnel–bridge sections

Weichao Yang, E. Deng, Xuhui He, Lusen Luo, Zhihui Zhu, Youwu Wang & Zhitang Li

To cite this article: Weichao Yang, E. Deng, Xuhui He, Lusen Luo, Zhihui Zhu, Youwu Wang & Zhitang Li (2021) Influence of wind barrier on the transient aerodynamic performance of high-speed trains under crosswinds at tunnel–bridge sections, Engineering Applications of Computational Fluid Mechanics, 15:1, 727-746, DOI: 10.1080/19942060.2021.1918257

To link to this article: https://doi.org/10.1080/19942060.2021.1918257

Published online: 03 May 2021.

ENGINEERING APPLICATIONS OF COMPUTATIONAL FLUID MECHANICS
2021, VOL. 15, NO. 1, 727–746
https://doi.org/10.1080/19942060.2021.1918257

Taylor & Francis
Taylor & Francis Group

Influence of wind barrier on the transient aerodynamic performance of high-speed trains under crosswinds at tunnel–bridge sections

Weichao Yang[a,b], E. Deng [a], Xuhui He[a,b], Lusen Luo[c], Zhihui Zhu[a,b], Youwu Wang[d] and Zhitang Li[e]

[a]School of Civil Engineering, Central South University, Changsha, People's Republic of China; [b]National Engineering Laboratory for Construction Technology of High Speed Railway, Changsha, People's Republic of China; [c]China Railway Eryuan Engineering Group Co., LTD., Chengdu, People's Republic of China; [d]Department of Civil and Environmental Engineering, The Hong Kong Polytechnic University, Kowloon, Hong Kong, People's Republic of China; [e]Poly Changda Engineering Co., LTD, Guangzhou, People's Republic of China

ABSTRACT

Porous wind barriers (PWBs) are gradually applied to tunnel–bridge–tunnel infrastructures (TBTIs) along high-speed railway lines. Due to the remarkable aerodynamic effect of high-speed trains (HSTs), the windproof performance of a PWB at tunnel–bridge section (TBS) is particularly critical when a HST passes through the TBTI under crosswind. And it seems to be easily ignored by researchers. This study aims to determine the influence mechanism of the PWB in the TBS. A CFD dynamic model of air–train–PWB was built based on porous media theory, and its reliability is verified by model and field tests. The main results are as follows: the corresponding variation amplitudes of the train's aerodynamic load coefficients are reduced by 36–95% when a PWB is set in the TBS; adopting the same design parameters along the full-length PWB on the TBTI is unreasonable; the PWB height and porosity in the TBS must be increased and reduced more than 33%, respectively, to achieve equivalent windproof performance. The conclusions in this paper can provide a preliminary idea for the optimization design of the PWB on the TBTI.

ARTICLE HISTORY
Received 7 July 2020
Accepted 12 April 2021

KEYWORDS
Crosswind; porous wind barrier (PWB); tunnel–bridge section (TBS); high-speed train (HST); aerodynamic coefficient

1. Introduction

In mountainous areas, tunnel–bridge section (TBS) has become the most common infrastructure scenario for high-speed railway (HSR) lines crossing canyons (Li et al., 2019; Olmos & Astiz, 2018). For example, in the Lanzhou–Chongqing Railway Line, bridges and tunnels account for 70–80% of the total line length (Li et al., 2019; Liu et al., 2019). When the air from the open area flows into the canyon where two mountains face each other, this air will accelerate through the canyon and form the canyon wind (Li et al., 2017; Yu et al., 2019). Therefore, high-speed trains (HSTs) often encounter strong crosswind when they run to the tunnel–bridge–tunnel infrastructure (TBTI). Chen et al. (2019) used driving simulators and observed that the running stability of a box truck is considerably worse when it runs to a TBS under crosswind, even if its running speed is far lower than that of an HST. Deng et al. (2019), Deng, Yang, Deng, et al. (2020), Deng, Yang, He, et al. (2020) also found that the train body experiences a strong aerodynamic impact when an HST drives into (or out of) a tunnel under crosswind. This situation seriously threatens the safety of train running. Porous wind barriers (PWBs) are gradually applied to bridges in this area to improve the running safety of the HST and the structure stability of the bridge (Figure 1).

Many researchers have conducted a series of research on the aerodynamic effect of PWBs in the bridge section (BS) in recent years. However, they mainly focused on the steady or quasi-steady-state process when a vehicle runs completely into the PWB section of a bridge and did not involve the transformation of infrastructure scenarios during the running process. For example, Avila-Sanchez et al. (2016) used the particle image velocimetry method to observe the effect of a solid wind barrier on the transverse streamline characteristics around the bridge. Xiang et al. (2018) studied the effect of the height of a solid windbreak on the aerodynamic loads of a cuboid vehicle moving on a bridge through an indoor test and discussed the difference in the results of static and dynamic models. The relative motion between the train and windbreak will intensify the aerodynamic effect of the train, and the aerodynamic loads acting on the train will decrease with increasing barrier height. Kozmar et al. (2012, 2014) studied the effect of the porosity and height of a PWB on the flow field characteristics of trains running on a bridge through an indoor test. A set of optimal parameters of the PWB, namely, porosity of 30% and height of

CONTACT E. Deng denge12@csu.edu.cn

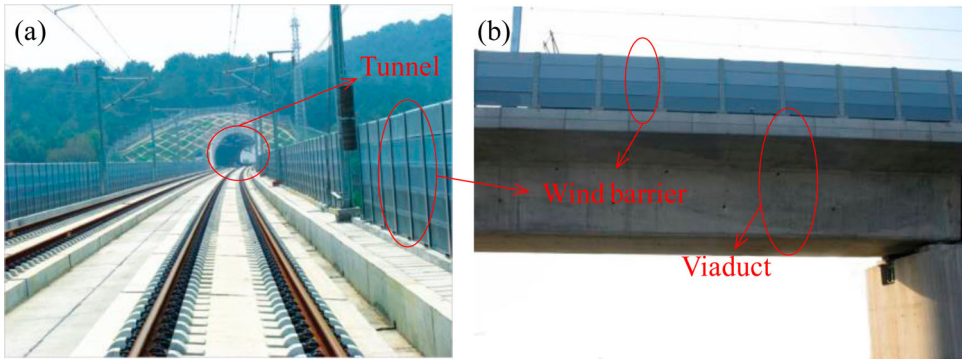

Figure 1. Typical PWB at a bridge–tunnel section.

5 m, was obtained. Chen et al. (2015) studied the influence of PWBs with different pore types on the running safety of road vehicles running on a bridge by establishing a large-scale wind tunnel test model. He, Fang, et al. (2019) studied the influence of a louver-type PWB on the aerodynamic characteristics of a vehicle–bridge based on a wind tunnel experiment and optimized its parameters.

The windproof performance of a PWB in a TBS is particularly critical when an HST runs in this section under the condition of crosswind. The simulation of a PWB is the key link. A PWB (especially the louver type) is simulated by scale model test due to the heavy workload of establishing its 3D numerical model (Xiang et al., 2018). For example, Telenta et al. (2014) and He et al. (2016) and studied the aerodynamic performance of an adjustable louver PWB through a wind tunnel test. However, the relative motion between train and PWB is difficult to realize in an indoor test, especially for the study of the transient flow field in the HST running process. The numerical simulation method is used in the study of solid windbreak. Liu et al. (2018), Niu, Zhou, and Liang, (2018) and Niu, Zhou, and Wang (2018), for example, studied the influence of windbreaks on the aerodynamic performance of HSTs running on embankment (or flat ground) based on the shear-stress transport (SST) k-ω turbulence model. Although a few researchers (Bendjebbas et al., 2018; He, Zhou, et al., 2019; Telenta et al., 2014) have used numerical methods to simulate the complex PWBs, they are limited to the 2D characteristics of the flow field. For the traditional vertical PWB (e.g. porous or fence-type) that is widely used in a TBS, porosity and height are the main factors affecting its windproof performance (He, Zhou et al., 2019; Kozmar et al., 2014). The effect of the pore form on the train's aerodynamic characteristics is limited if the porosity and height are the same (Xiang et al., 2013). Therefore, a porous medium model is an economical, efficient and satisfying choice for simulating a PWB approximately aiming at the transient aerodynamic effects of trains in the TBS.

Based on a typical TBTI along a HSR in China, this study completes the following works. Firstly, A CFD dynamic model of air–train–PWB was built based on the porous media theory, and its reliability is verified by model and field tests. Secondly, the transient aerodynamic load coefficients and the change in carriage-running postures in the critical process are the objects, and the differences in aerodynamic performance when a train runs on this infrastructure under crosswind with or without PWBs are compared. Thirdly, aiming at the process in the TBS (i.e. the process of the HST passing from the tunnel to the bridge or vice versa), the influence mechanism of the existence of a PWB on the transient aerodynamic effect is determined from the viewpoint of the field of flow. Fourthly, the influences of the porosity (α) and height (H) of the PWB on the transient aerodynamic performance of the HST are discussed. The conclusions in this paper can provide a preliminary idea for the optimization design of the PWB on the TBTI.

2. Basic theory

2.1. Turbulence model

The estimated maximum Mach number (Ma) is less than 0.3, and the corresponding Reynolds number (Re) is greater than 1×10^6 in accordance with the background of this study. The air flow involved is incompressible and highly turbulent. The Detached eddy simulation (DES) method is the current mainstream for solving the flow field with higher Re. (Chen et al., 2016; Guo et al., 2020; Li et al., 2020). Based on the SST κ–ω turbulent model, delayed DES method (DDES) was applied in the present paper because it can further prevent the separation of premature flow based on DES (Niu, Zhou, & Wang, 2018). The SST k-ω turbulence model (Niu, Zhou, & Liang, 2018; Ramezanizadeh et al., 2019) was used to simulate the region near the train surface, as shown

below:

$$\frac{\mathrm{D}\rho k}{\mathrm{D}t} = \frac{\partial}{\partial x_j}\left[(\mu + \sigma_k \mu_t)\frac{\partial k}{\partial x_j}\right] + \tau_{ij}\frac{\partial u_i}{\partial x_j} - \beta^* \rho \omega k, \tag{1}$$

$$\frac{\mathrm{D}\rho \omega}{\mathrm{D}t} = \frac{\partial}{\partial x_j}\left[(\mu + \sigma_\omega \mu_t)\frac{\partial \omega}{\partial x_j}\right] + \frac{\gamma}{\nu_t}\tau_{ij}\frac{\partial u_i}{\partial x_j} - \beta \rho \omega^2 + 2(1 - F_1)\rho \sigma_{\omega 2}\frac{1}{\omega}\frac{\partial k}{\partial x_j}\frac{\partial \omega}{\partial x_j}, \tag{2}$$

$$\tau_{ij} = -\rho\overline{u_i' u_j'} = \mu_t\left(\frac{\partial u_i}{\partial x_j} + \frac{\partial u_j}{\partial x_i} - \frac{2}{3}\frac{\partial u_k}{\partial x_k}\delta_{ij}\right) - \frac{2}{3}\rho k \delta_{ij}, \tag{3}$$

$$\nu_t = \frac{a_1 k}{\max(a_1 \omega;\ \Omega F_2)}, \tag{4}$$

$$F_2 = \tanh(\arg_2^2), \tag{5}$$

$$\arg_2 = \max\left(2\frac{\sqrt{k}}{0.09\omega y};\ \frac{500\nu_t}{y^2 \omega}\right), \tag{6}$$

$$F_1 = \tanh(\arg_1^4), \tag{7}$$

$$\arg_1 = \min\left(\max\left(\frac{\sqrt{k}}{0.09\omega y};\ \frac{500\nu_t}{y^2\omega}\right);\ \frac{4\rho\sigma_{\omega 2}k}{CD_{k\omega}y^2}\right), \tag{8}$$

$$CD_{k\omega} = \max\left(2\rho\sigma_{\omega 2}\frac{1}{\omega}\frac{\partial k}{\partial x_j}\frac{\partial \omega}{\partial x_j};\ 10^{-20}\right), \tag{9}$$

where ρ is the density of the air flow; u represents the velocity of the flow; Ω is the vorticity; y represents the distance from the wall; ν_t represents the eddy viscosity; μ_t represents the viscosity of turbulence; k represents the turbulence kinetic energy; δ is the Kronecker delta; and F_2 are the blending functions; the subscripts i and j represent the directions; a_1, σ_k, σ_ω, β, β^*, ω and γ are the empirical parameters.

2.2. Porous media model

This study only focuses on the flow field characteristics of the leeward side after the air flows through the PWB. The flow state of the airflow inside the PWB can be ignored. Thus, the porous medium model is used to simulate the PWB. The specific implementation method is typically used to add a source term representing the momentum consumption to the fluid momentum equation (Rosenfeld et al., 2010) as follows:

$$\begin{cases} \frac{\partial u_i}{\partial x_i} = 0 \\ \rho\frac{\partial u_i}{\partial t} + \rho u_j \frac{\partial u_i}{\partial x_j} \\ = -\frac{\partial p}{\partial x_i} + \nu\rho\left(\frac{\partial^2 u_i}{\partial x_j \partial x_i} + \frac{\partial^2 u_j}{\partial x_i \partial x_j}\right) + \frac{\partial}{\partial x_i}(S_i) \end{cases}, \tag{10}$$

where u represents the velocity vector of the air; x represents the scale vector; the subscript $i, j = 1, 2, 3$ represent three directions; p represents the aerodynamic pressure; ν represents the kinematic viscosity of the air; ν represents the density of the air; and S_i represents the additional source terms.

The additional source terms can be written as follows:

$$S_i = -\left(\sum_{j=1}^{3}\frac{\mu}{k_{ij}}\frac{\partial u_j}{\partial t} + \sum_{j=1}^{3} C_{ij}\frac{1}{2}\rho|u_j|u_j\right) = -\left(\sum_{j=1}^{3} D_{ij}\mu\frac{\partial u_j}{\partial t} + \sum_{j=1}^{3} C_{ij}\frac{1}{2}\rho|u_j|u_j\right), \tag{11}$$

where μ represents the dynamic viscosity of the air; k_{ij} represents the seepage coefficient; D_{ij} represents the viscous resistance coefficient; and C_{ij} represents the inertial resistance coefficient.

The additional source terms consist of viscous and inertial loss terms. For the perforated plate, when the incoming flow from a single direction is vertical through it, the internal air cannot flow along the plane direction. In other words, the flow velocities in the two directions perpendicular to the incoming flow direction in Equation (11) are zero. Therefore, on the premise that the incoming flow direction is fixed, this paper only simplifies the momentum additional source terms in the incoming flow direction. Furthermore, due to the very large seepage coefficient in the thickness direction (estimated to be about 10^7–10^8 m/s) in the perforated plate, the viscous resistance coefficient is almost zero, and only the inertial loss term is retained. Equation (11) can be rewritten as follows:

$$S_1 = -\left(\sum_{j=1}^{3} C_j\frac{1}{2}\rho|u_j|u_j\right) \approx -\left(C_2\frac{1}{2}\rho|u_2|u_2\right), \tag{12}$$

where the inertial resistance coefficient C_2 in the incoming flow direction is closely related to the α of the PWB, which can be calculated in accordance with the test method in Figure 2. The formula is as follows:

$$p_u - p_d = C_2\frac{1}{2}\rho|u_2|u_2. \tag{13}$$

Various researchers have presented different inertial resistance coefficient models through experiments. Three models (Yeh et al., 2010), i.e. Reynolds, Hoerner and Bailey, are commonly used and are respectively represented by the following Equations (14)–(16). According to Deng et al. (2021), the Reynolds model is applied in this paper to simulate porous media.

$$C_2 = 1.04(1 - \alpha^2)/\alpha^2 \tag{14}$$

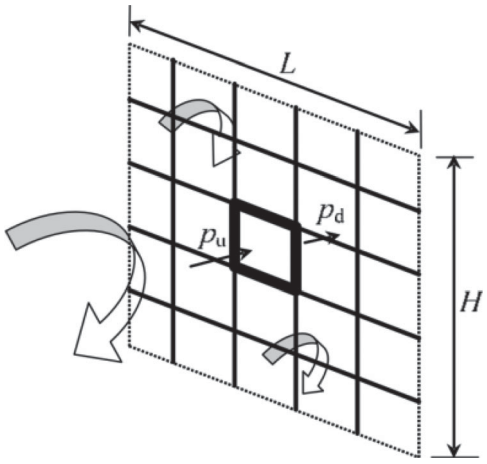

Figure 2. Schematic of pressure reduction measurement.

$$C_2 = \frac{1}{2}\left(\frac{3}{2\alpha} - 1\right)^2 \tag{15}$$

$$C_2 = \left(\frac{1-\alpha^2}{\alpha^2}\right)\left[\frac{18}{Re} + \frac{0.75}{\lg(Re+1.25)} + 0.055\lg(Re)\right] \tag{16}$$

2.3. Dimensionless aerodynamic forces and moments

A scheme for calculating aerodynamic forces and moments has been proposed and verified in Deng, Yang, Deng, et al. (2020). The corresponding dimensionless calculation formula is shown below. The definition of each symbol is given in Deng et al. (2021).

$$\begin{aligned} C_P &= (P - P_\infty)/(0.5\rho {V_a}^2) \\ C_i &= F_i/(0.5\rho V_a^2 A) \\ C_{mi} &= M_i/(0.5\rho V_a^2 A h). \end{aligned} \tag{17}$$

3. Information for numerical model

3.1. Geometry and boundary conditions

The CRH3 train commonly used in China's HSRs is adopted as the train model in the present study. The geometric model of the real HST is simplified to a certain extent (Figure 3(a)). Bogie, pantograph and window are ignored. It is composed of three carriages (i.e. the head, middle and tail carriages), with a total length of approximately 76 m (Figure 3(b, c)). The geometric model of the bridge is based on a concrete simply supported box girder (Figure 4). The length and height of the bridge are 159 and 3.05 m, respectively. The deck width is 12.0 m. The track structure on the bridge deck and piers is ignored. The bottom of the HST is 0.2 m from the bridge deck. The PWB thickness (D) is 0.1 m. Its H varies from 2.5 m to 4.0 m, and the α varies from 20% to 40%. The two ends of the bridge are connected with two double-line tunnels (Tunnels 1 and 2).

The overall calculation zone is shown in Figure 4(a). The starting point of the HST head is approximately 80 m

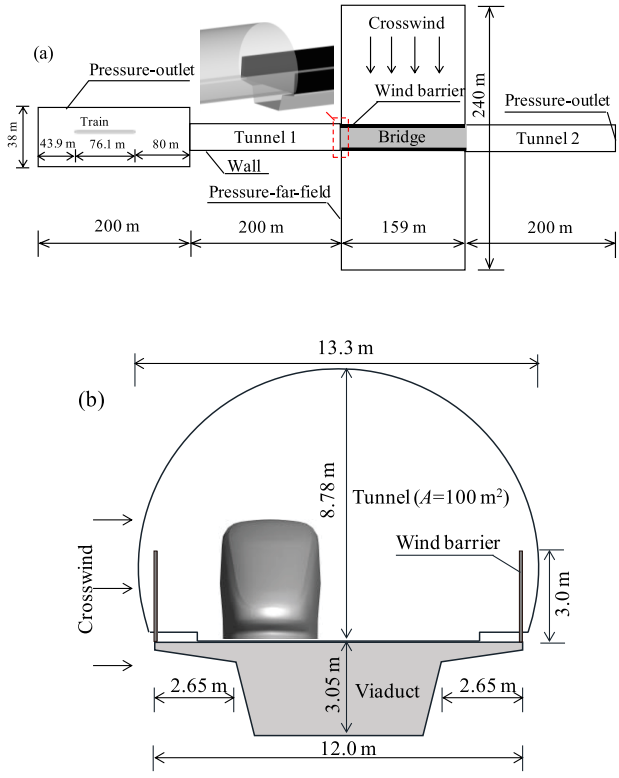

Figure 4. Computational domain: (a) top view and (b) the cross-section of the bridge–tunnel section.

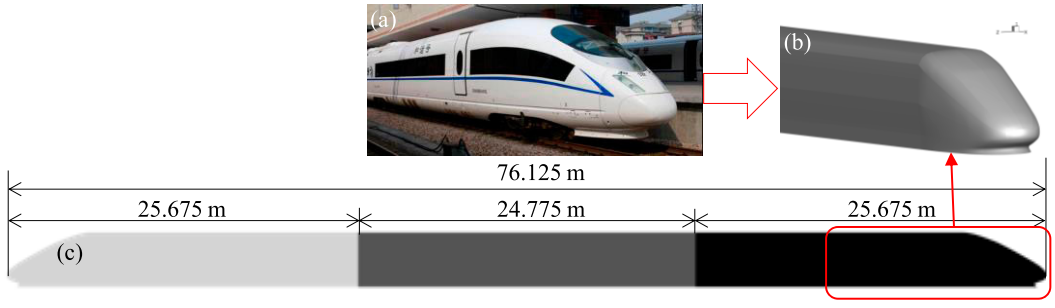

Figure 3. Train geometric model: (a) physical photograph, (b) head carriage model and (c) side view.

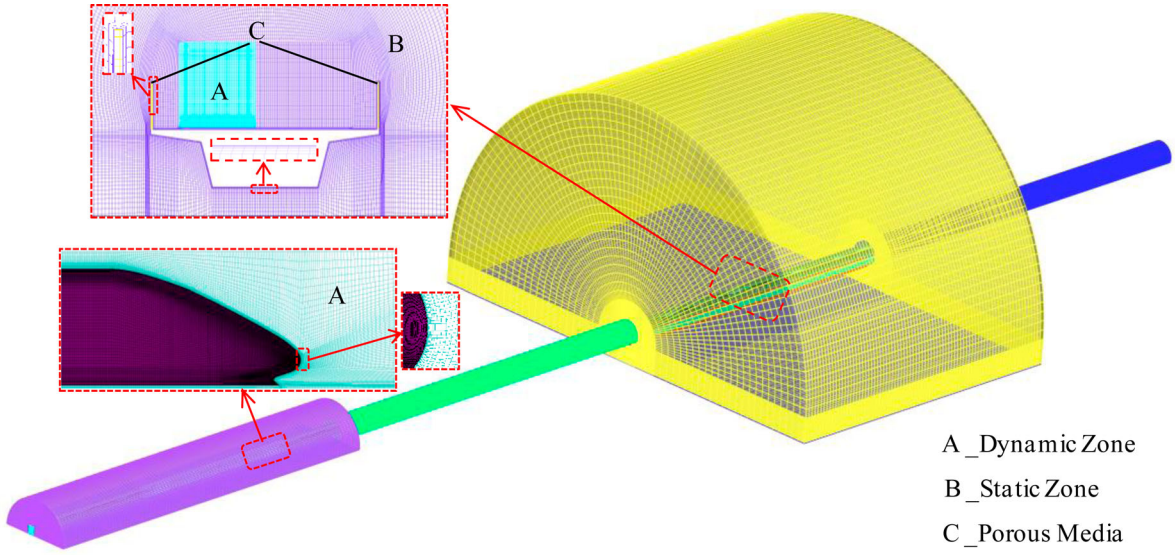

Figure 5. Grid model.

from Tunnel 1 inlet. The train running speed (V_t) is set to 250 km/h. The atmospheric field at both ends of Tunnel 1 is a semi-infinite space simulated by a semi-cylinder. The outside of Tunnel 1 inlet is flat ground, and the corresponding atmospheric field has a diameter of approximately 38 m and a length of 200 m. No crosswind occurs, and pressure-outlet boundary conditions are adopted. The atmospheric field in the BS is approximately 240 in diameter, and pressure-far-field boundary conditions are adopted. The crosswind velocity relative to the ground (V_w) is set to 25 m/s and is perpendicular to the bridge. The pressure-outlet boundary condition is also used at Tunnel 2 outlet. Nonslip wall boundary conditions are applied to the surface of the train and the bridge, the wall of tunnels and the ground.

3.2. Mesh strategy and solution scheme

The mesh model is shown in Figure 5. In the present paper, the porous medium zone (corresponding to PWB) is added on the basis of mesh model in Deng, Yang, He et al. (2020). An 8-layers prism grid is generated on the PWB surface (Mou et al., 2017). The y^+ value is about 10. The model has approximately 32 million grid cells. Based on the ANSYS FLUENT, the discretised equations are solved by the semi-implicit approach (Yang et al., 2018). The size of time-step for calculation is fixed at 1×10^{-4} s.

4. Verification

4.1. Verification of partition scheme independence

The purpose of this section is to choose a reasonable aerodynamic coefficient calculation scheme that can also balance the efficiency and accuracy of the calculation. Among them, the number of longitudinal sections is fixed at 20, and the number of circumferential faces is increased from 6 to 48. The corresponding results have been given in Deng, Yang, He, et al. (2020). The results show that the scheme with 24 circumferential calculation faces is appropriate.

4.2. Analysis of mesh sensitivity

In this section, the calculation results of 3 models with different mesh element numbers (16, 32 and 48 millions) are compared. The 3 models were established by reducing the longitudinal size of the grids, and other conditions (e.g. the height of the first boundary layer near the train) remained the same. Other parameters and processes are consistent with Deng, Yang, He, et al. (2020). Figure 6

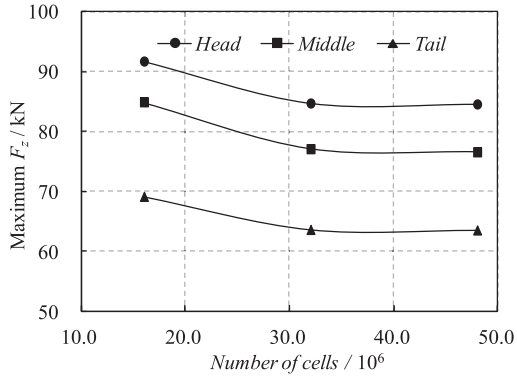

Figure 6. Maximum side forces of three carriages at different longitudinal mesh resolutions.

shows the comparison results. The results show that the quantity of mesh cells is reasonable at 32 million.

5. Differences in aerodynamics with or without PWBs

5.1. Aerodynamic coefficients

Figure 7 shows the time-histories of the aerodynamic coefficients when a HST runs on the TBTI with or without PWB. The H and α of the PWB are 3.0 m and 30%, respectively. In the figure, 'OUT' means the time period when the HST leaves Tunnel 1 ($t = 4.02$–5.12 s); 'IN' means the time period when the HST enters Tunnel 2 ($t = 6.33$–7.43 s); the solid blue line indicates the case without PWB; and the solid red line indicates the case with PWB. Deng et al. (2019) showed that an obvious correlation exists between the fluctuation amplitude of the aerodynamic coefficient (C) and running safety. Table 1 shows the comparison of the peak C of three carriages in the two processes, with or without PWB. The schematic of the change behavior of the carriage's running posture in the 'OUT' and 'IN' processes is also given in Figure 7 to illustrate the fluctuation amplitude of aerodynamic coefficient vividly. Figure 7(a–e) shows the lateral movement, vertical movement, overturning movement on the cross-section, yawing movement on the horizontal plane, and the nodding movement on the vertical-section, respectively. Among them, Steps 1–4 are in strict chronological order, respectively. The distance between steps can qualitatively reflect the fluctuation amplitude of the corresponding aerodynamic load.

All the aerodynamic coefficients exhibit striking 'pulse' behavior in the 'OUT' and 'IN' processes under the condition without PWB. This phenomenon is similar to those reported in Yang et al. (2019), Yang, Deng, Zhu, He, et al. (2020), Yang, Deng, Zhu, Lei, et al. (2020). The three carriages also show complex posture change behavior, which is composed of lateral movement, jump, overturn, deflection and nod, in the 'OUT' and 'IN' processes. The running safety and ride comfort in the 'OUT' and 'IN' processes are considerably poorer than those in other periods, when the HST driving on the TBTI in the absence of a PWB on the bridge.

The C in the 'OUT' and 'IN' processes decrease considerably under the condition with PWB. The head carriage is an example; the peak fluctuation amplitudes of C_z, C_y, C_{mx}, C_{my} and C_{mz} decrease by 86%, 82%, 80%, 59% and 36%, respectively, in the 'OUT' and by 87%, 83%, 83%, 61% and 61%, respectively, in the 'IN'. The amplitude and step number of the running posture change behavior of each carriage are consequently reduced considerably. For example, for the lateral movement, the head carriage changes from the original 'right to left' behavior to single 'left' behavior in the 'IN' process (Figure 7(a_1)). For the jump behavior, the middle carriage changes from the original 'up to down' behavior to single 'down' behavior in the 'IN' process (Figure 7(b_2)). For the deflection behavior, the front of the head carriage changes from the original 'right to left' behavior to single 'left' behavior in the 'OUT' process (Figure 7(d_1)). For the nod behavior, the rear of the tail carriage changes from the original 'up to down to up' behavior to a single 'down' behavior in the 'OUT' process (Figure 7(e_3)).

The reduction rate of the side force fluctuation amplitude of each carriage is more prominent compared with the other four aerodynamic coefficients under the condition with PWB, whether in the 'OUT' process or the 'IN' process. For example, the respective reduction rates of the head, middle and tail carriages are 86%, 95% and 87%in the 'OUT' process and 87%, 95% and 89% in the 'IN' process. The reduction rate of pitching moment fluctuation amplitude of the three carriages is relatively small. The change in aerodynamic side force of the HST when running in the TBS is most sensitive to the existence of a PWB, whereas the sensitivity of pitching moment is relatively weak.

The C and the corresponding step number of the running posture change behavior of each carriage in the 'IN' process are greater than those in the 'OUT' process under the condition without PWB. For example, for the lateral movement, the head carriage presents 'right to left' behavior in the 'IN' process but only single 'right' behavior in the 'OUT' process (Figure 7(a_1)). For the deflection behavior, the front of the head carriage presents 'right to left to right' behavior in the 'IN' process but only 'right to left' behavior in the 'OUT' process (Figure 7(d_1)). The ratio IN/OUT is applied to reflect the difference in the value of C in the 'OUT' and 'IN' processes. The IN/OUT values are greater than 1 under the condition without PWB. It's worth noting that the IN/OUT value is 1 for the case with PWB.

5.2. Flow field during the 'OUT' process

The influence mechanism of the existence of PWB on the train's aerodynamic sudden change effect is revealed from the perspective of flow field, aiming at the 'OUT' process, in this section. The horizontal plane $Y = 1.5$ m is an example. Figure 8 shows the comparison of the flow field in the 'OUT' process with or without PWB. The H and α of the PWB are 3.0 m and 30%, respectively. Figure 9 shows the streamline and pressure on several typical sections at $t = 4.58$ s for additional flow field information. The legend of pressure nephogram in Figure 9(b) is

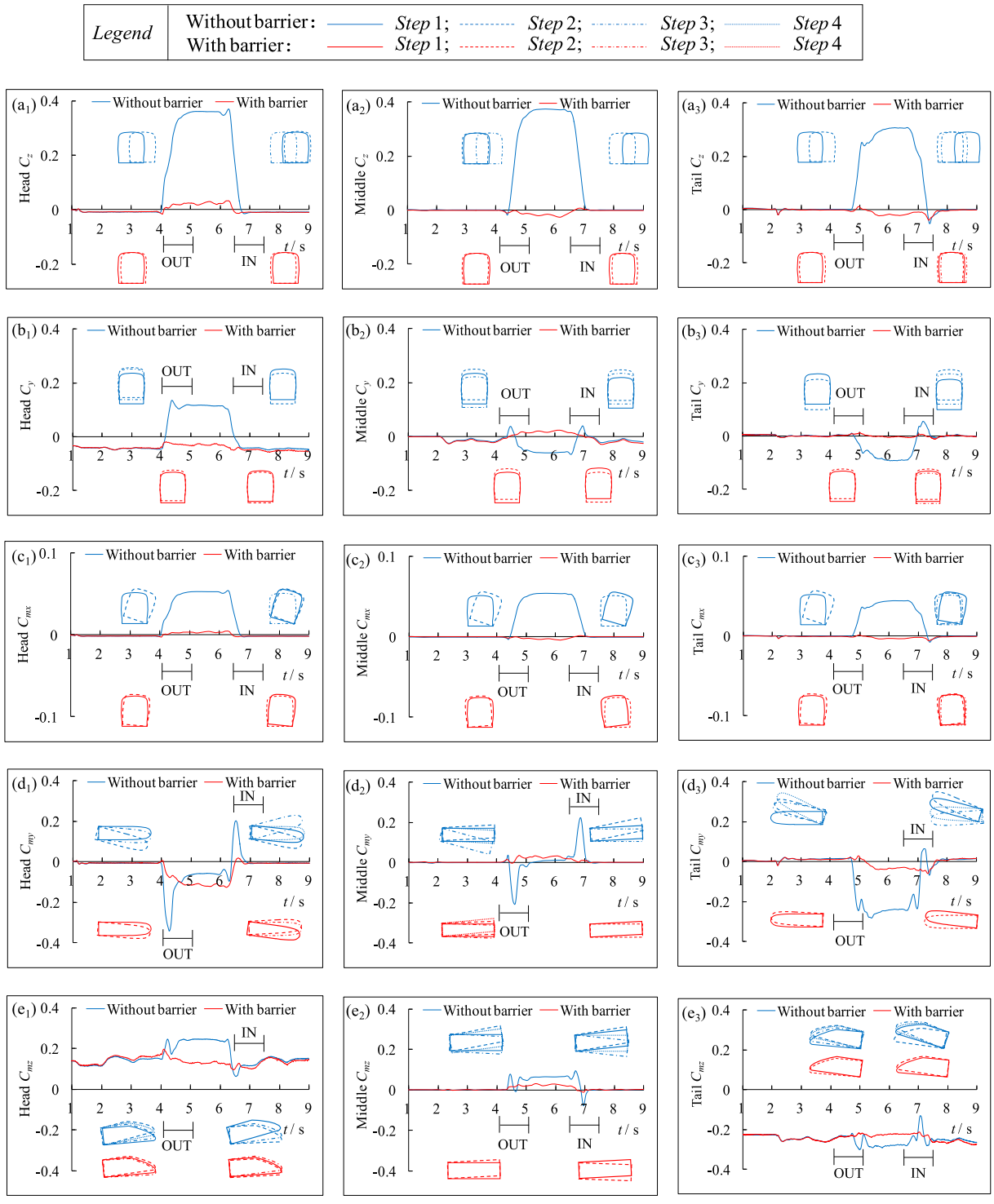

Figure 7. Comparison of the aerodynamic coefficients of each carriage with or without PWB: (a) side force, (b) lift force, (c) rolling moment, (d) yawing moment and (e) pitching moment ($V_t = 250$ km/h; $V_w = 25$ m/s).

consistent with that in Figure 8, Figure 9(c) is the pressure distribution on the contour line of $Y = 1.5$ m on the train surface. The following findings are obtained from Figures 8 and 9.

For the part of the train body within tunnel, the surrounding streamline and the pressure distribution on the train surface show similar characteristics, regardless of with or without the PWB. The airflow direction on two sides is opposite the train running direction and converges at the tail carriage tip. The pressures on two sides are roughly the same (negative), and the pressure value is basically the same. $t = 4.58$ s is used as an example.

Table 1. Comparison of the maximum fluctuation amplitudes of aerodynamic coefficients with or without wind barrier ($V_t = 250$ km/h; $V_w = 25$ m/s).

		OUT			IN			IN/OUT	
		Max(*C*)-Min(*C*)			Max(*C*)-Min(*C*)				
Cofficient	Carriage	Without barrier	With barrier	Reduction rate (%)	Without barrier	With barrier	Reduction rate (%)	Without barrier	With barrier
C_z	Head	0.37	0.05	86	0.38	0.05	87	1.03	1
	Middle	0.38	0.02	95	0.39	0.02	95	1.03	1
	Tail	0.31	0.04	87	0.36	0.04	89	1.16	1
C_y	Head	0.17	0.03	82	0.18	0.03	83	1.06	1
	Middle	0.09	0.04	56	0.11	0.04	64	1.22	1
	Tail	0.10	0.02	80	0.15	0.02	87	1.50	1
C_{mx}	Head	0.05	0.01	80	0.06	0.01	83	1.20	1
	Middle	0.06	0.01	83	0.06	0.01	83	1	1
	Tail	0.05	0.01	80	0.05	0.01	80	1	1
C_{my}	Head	0.32	0.13	59	0.33	0.13	61	1.03	1
	Middle	0.23	0.04	83	0.24	0.04	83	1.04	1
	Tail	0.30	0.07	77	0.31	0.07	77	1.03	1
C_{mz}	Head	0.11	0.07	36	0.18	0.07	61	1.64	1
	Middle	0.09	0.03	67	0.17	0.04	76	1.89	1.33
	Tail	0.08	0.05	38	0.15	0.07	53	1.88	1.40

The pressure distribution on the train surface (S1 and S2 in Figure 9(b)) within the tunnel is even, and the pressure coefficient values are maintained between −0.1 and −0.2. The PWB on the bridge has a minimal effect on the flow field and pressure within Tunnel 1.

For the part of the train body on the bridge, a large longitudinal horn-shaped vortex is generated on the leeward side by the combined action of the side flow and the train slip-stream under the condition without PWB (Figure 8(a_1–g_1)). The vortex zone corresponds to the negative pressure zone. $t = 4.58$ s is taken again as an example; the maximum negative pressure coefficient flat train surface is about −0.2 (Leeward side, Figure 9(c)). The positive pressure is uniformly distributed along the longitudinal direction on the windward side of the flat train surface under the front extrusion of the crosswind, and the corresponding value is approximately 0.1 (e.g. S4 and S5 in Figure 9(b)). This condition is the main reason for the considerable lateral movement and deflection behavior of the middle carriage in the 'OUT' process (Figure 7(a_2 and d_2)). A towering negative pressure zone exists at the junction of the windward surface and roof on the flat train body due to the rapid increase in the crosswind flow velocity when it bypasses the windward surface (S5 in Figure 9(b), the maximum negative pressure coefficient can reach approximately −0.5). It is also the main reason for the obvious jump, overturn and nod behavior of the middle carriage in the 'OUT' process (Figure 7(b_2, c_2 and e_2)). The difference of the pressure between the leeward and windward sides is greatest at the head carriage tip. The peak positive and negative pressure coefficients are 0.4 and −0.7, respectively, as shown in Figure 9(c).

Under the condition with PWB, the area between the PWB and the train body is a negative-pressure zone (Figure 8(a_2–g_2)). With $t = 4.58$ s as an example, the negative pressure is distributed on the flat train surface under the windproof effect of the PWB, even if some streamlines penetrate the PWBs on both sides and collect at the HST's leeward side to form a large vortex. The corresponding negative pressure coefficient values are maintained between −0.1 and −0.2, which are consistent with the values on the train surface within Tunnel 1 (S1–S5 in Figure 9(b)). The pressure difference at the head carriage tip is also considerably weakened, with the maximum positive and negative pressure coefficients falling to 0.2 and −0.3, respectively (Figure 9(c)). In other words, the difference in the longitudinal distribution of the pressure on the carriage surface is remarkably reduced. Therefore, the aerodynamic coefficient fluctuation amplitudes are greatly reduced in the 'OUT' process. The aerodynamic side force of each carriage is most sensitive to the influence of the existence of PWB, because the PWB weakens the kinetic energy of crosswind flow in the transverse direction.

5.3. Flow field during the 'IN' process

Figure 10 shows the comparison of the flow field in the 'IN' process with or without PWB. The remaining conditions remain the same as in the previous section. For detailed flow field information, Figure 11 shows the streamline and pressure on several typical sections at $t = 6.87$ s. The legend of pressure nephogram in Figure 11(b) is consistent with that in Figure 10. Figure 11(c) is the pressure distribution on the contour line of $Y = 1.5$ m on the train surface. The following findings are obtained from Figures 10 and 11.

The PWB on the bridge has a minimal effect on the streamline and pressure on the train body within Tunnel

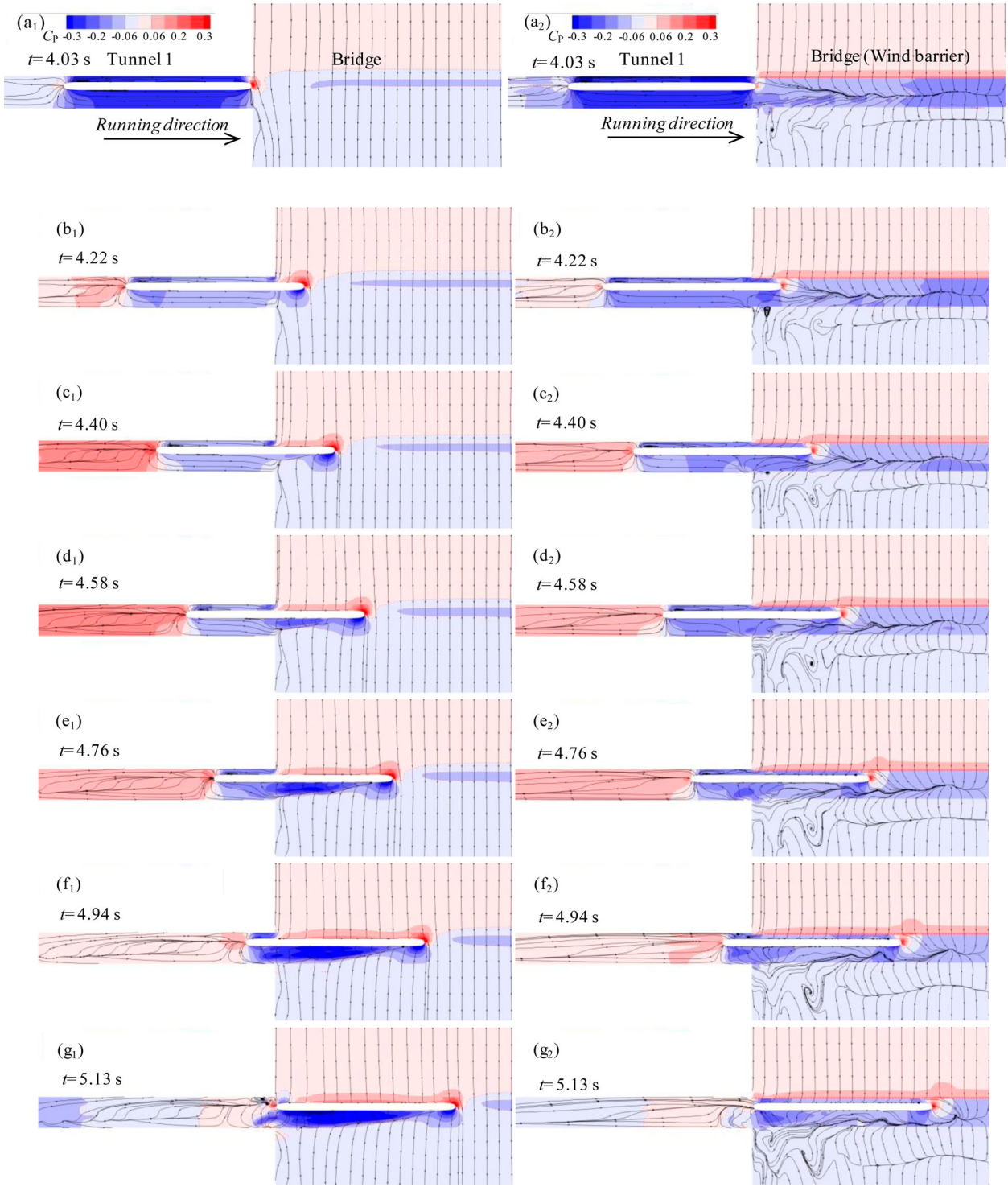

Figure 8. Comparison of flow field evolution on the horizontal plane $Y = 1.5$ m in the 'OUT' process with (a_2–g_2) or without (a_1–g_1) PWB ($V_t = 250$ km/h; $V_w = 25$ m/s).

2. The streamline at the head carriage tip presents a source flow characteristic, regardless of with or without the PWB. The area near the head carriage tip is a strong positive pressure zone, because it is compressed; the air in front of the head carriage flows forward; the other part of the air flows out at Tunnel 2 inlet along the gap between the carriage and tunnel, forming a jet flow. The direction of the jet flow is approximately parallel to the longitudinal direction of the tunnel before it ejects the tunnel entrance (Figure 10(a_1–g_1)). The pressure in the gap area between the train body and tunnel is evenly distributed along the longitudinal direction, and the pressure values on both

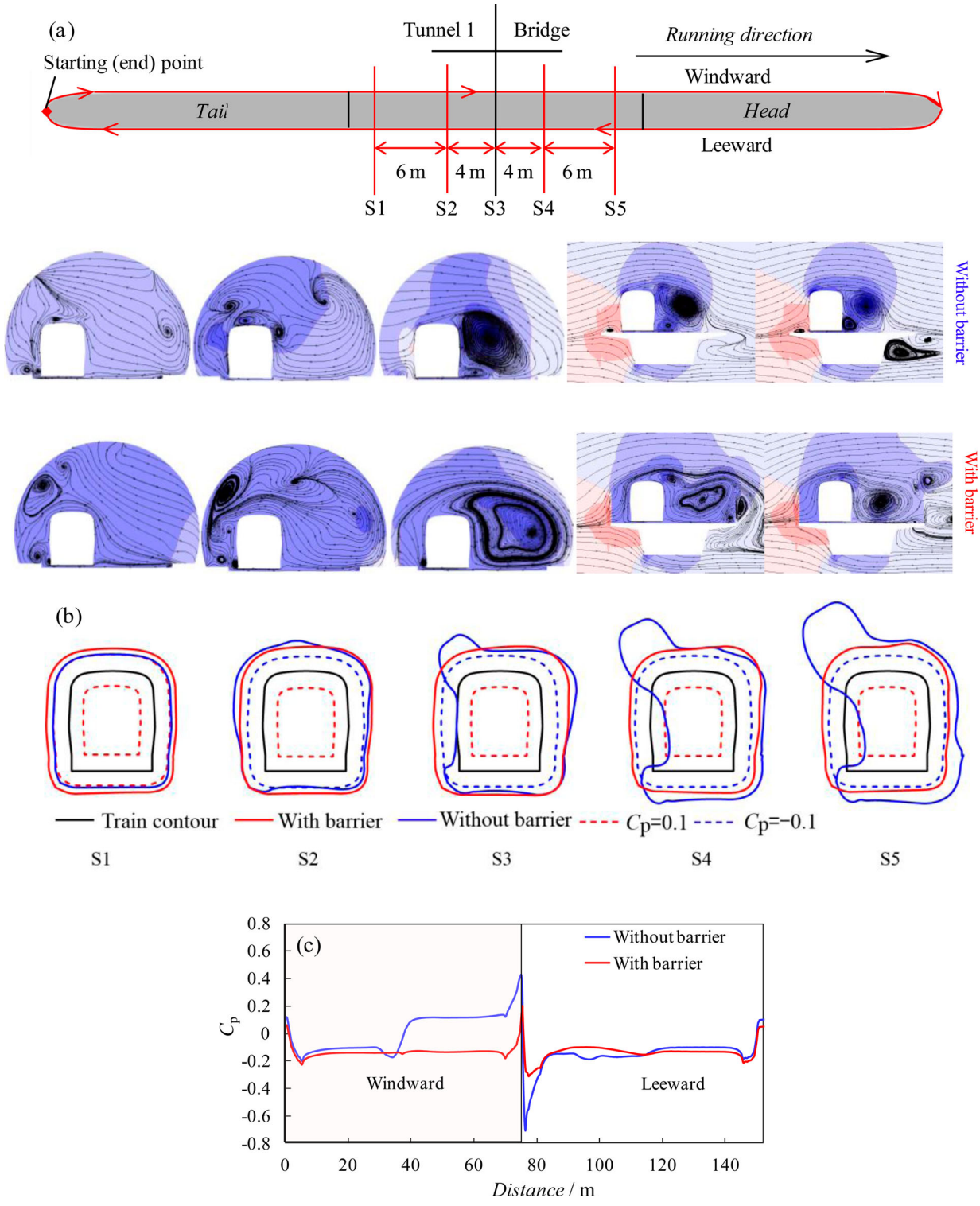

Figure 9. Comparison of flow information on the typical section with or without PWB at $t = 4.58$ s: (a) location of typical section, (b) flow field and pressure distribution on typical cross-section and (c) pressure distribution of the train body on the horizontal plane $Y = 1.5$ m ($V_t = 250$ km/h; $V_w = 25$ m/s).

sides are basically equal. $t = 6.87$ s is used as an example. The pressure on the two sides of the HST within Tunnel 2 is symmetrically distributed, with head carriage tip as the center (Figure 11(c)). The positive peak of the pressure coefficient (approximately 0.6) appears at the head carriage tip. The pressure on the flat train surface is evenly distributed, and the pressure coefficient values are kept near 0 (S4 and S5 in Figure 11(b)).

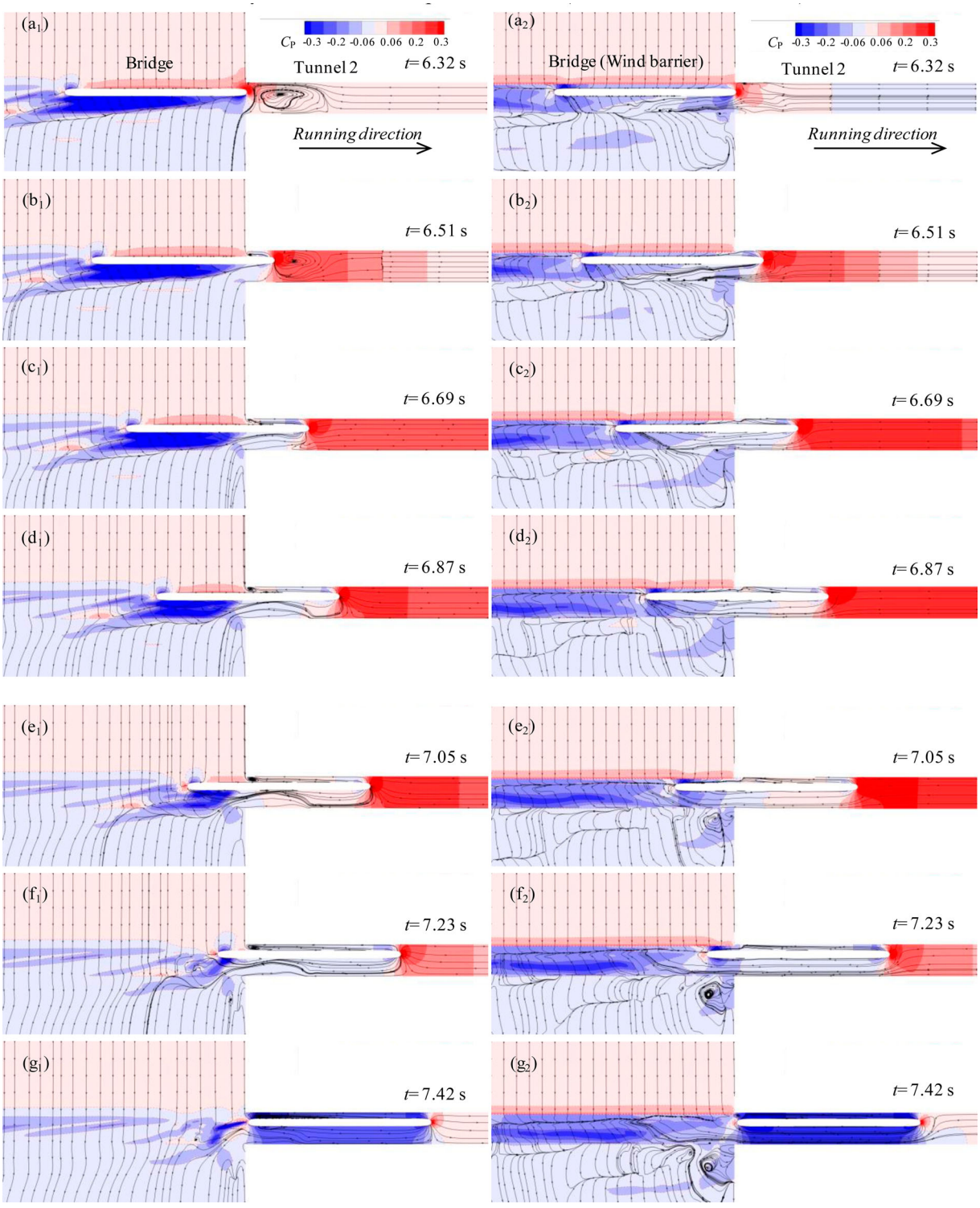

Figure 10. Comparison of flow field evolution on the horizontal plane $Y = 1.5$ m in the 'IN' process with (a_2–g_2) or without (a_1–g_1) PWB ($V_t = 250$ km/h; $V_w = 25$ m/s).

For the part on the bridge without PWB, the transverse airflow circumvents the carriage top and creates longitudinal vortexes on the leeward side of the train. It appears as a horn under the combined effect of the train wind (Figure 10(a_1)). The triangular negative pressure area corresponds to the longitudinal horn-shaped vortex area, and the negative pressure value also changes with the shape of the vortex. Under the suppression of

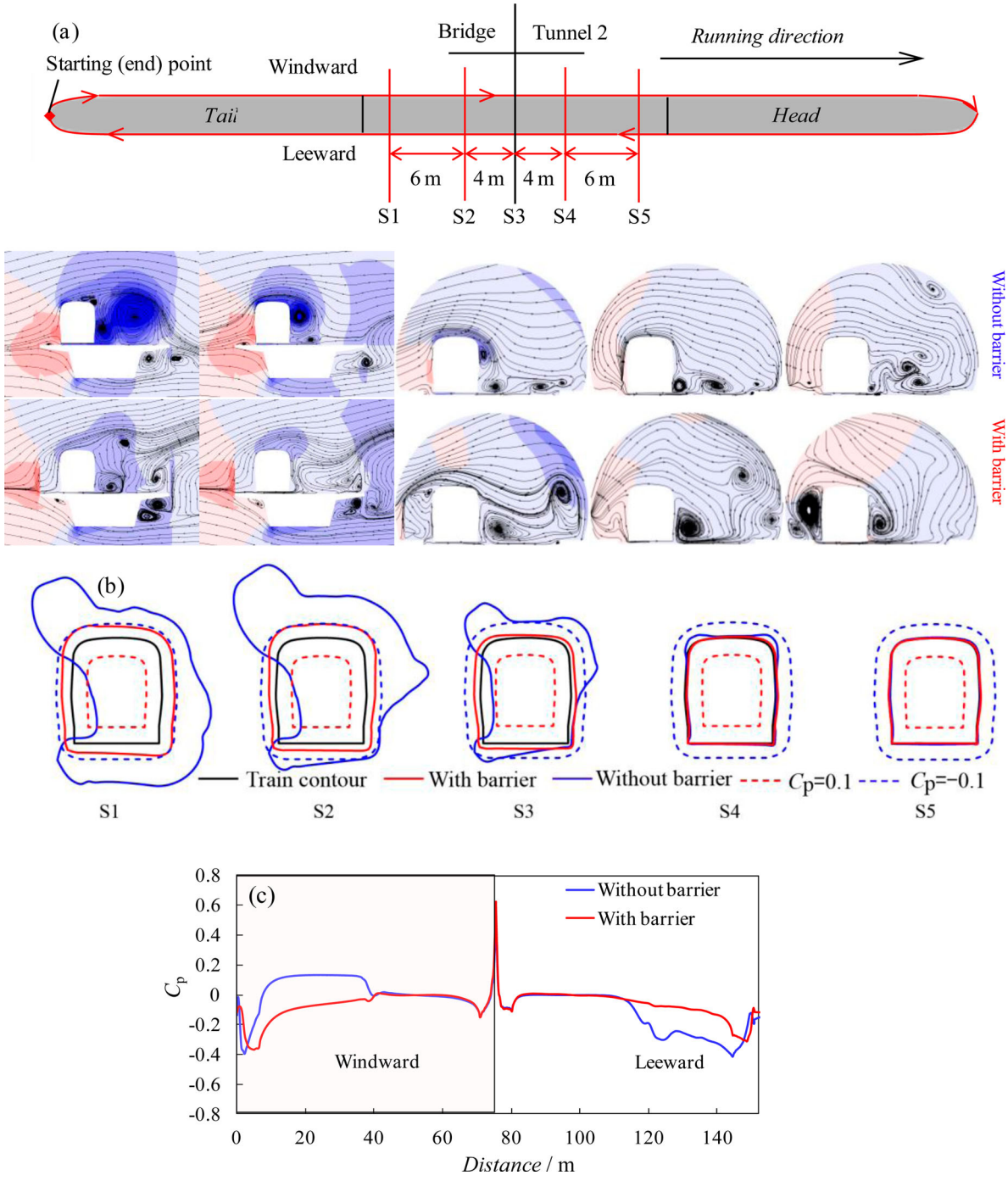

Figure 11. Comparison of flow information on the typical section with or without PWB at $t = 6.87$ s: (a) location of typical section, (b) flow field and pressure distribution on typical cross-section and (c) pressure distribution of the train body on the horizontal plane $Y = 1.5$ m ($V_t = 250$ km/h; $V_w = 25$ m/s).

jet flow, the horn-shaped vortex stops at the entrance of Tunnel 2 with the train entering. The direction of the jets near the entrance changed to some extent, and the residual longitudinal vortex attached to the train leeward surface expanded to a certain extent (Figure 10(b_1–g_1)). Consequently, the negative pressure acting on the train leeward surface is greater than the corresponding value in the 'OUT' process. Given $t = 6.87$ s, the negative pressure coefficient at the leeward side of S1 and S2 sections in Figure 11(b) is greater than that of S4 and S5 sections in Figure 9(b). The jet flow on the windward side dissipates at the inlet of Tunnel 2, because it combines with the crosswind to produce vertical vortex (Figure 10(b_1–g_1)). Therefore, the jet flow has little effect on the positive

pressure on the windward side. The positive pressure coefficient on the flat HST surface outside the tunnel remains at approximately 0.1 (Figure 11(c)). The main reason for the fact that the train's aerodynamic coefficient fluctuation amplitudes in the 'IN' process are greater than those in the 'OUT' process under the condition without PWB may be that the residual longitudinal eddy expands radially under the longitudinal extrusion of the jet flow.

The squirt flow from Tunnel 2 entrance converges at the tail carriage tip under the condition with PWB (Figure 10(c_2–g_2)). The interference of crosswind to the streamline structure between the two PWBs is considerably weakened. With $t = 6.87$ s as an example, the pressures on the two sides of the HST outside the tunnel remain symmetrical, and the pressure coefficient values on the flat train surface are maintained between 0 and −0.1 (S1–S3 in Figure 11(b)). Therefore, the train's aerodynamic coefficient fluctuation amplitudes are considerably reduced compared with the corresponding values under the condition without PWB in the 'IN' process.

6. Effect of PWB parameters

6.1. Effect of height

This section discusses the effect of PWB height on the transient aerodynamic performance of the train. Figure 12 shows the variation of the aerodynamic coefficients (solid lines) as the train runs on the TBTI at different PWB heights ($H = 2.5$, 3.0, 3.5, 4.0 m; $\alpha = 30\%$). The corresponding values are based on the left ordinate.

A train is a vibrational system with multiple degrees of freedom. Transient aerodynamic loads will threaten the safety of the train during operation (Li et al., 2015). The running safety of the HST was evaluated by the change rate of the aerodynamic coefficient ($\Delta C'_{(0.035s)}$, Deng, Yang, He, et al., 2020). The $\Delta C'_{(0.035s)}$ variations are presented as the dashed lines in Figure 12. Here 'OUT' and 'IN' are defined as in Figure 9, and 'BR' denotes the period of the HST running only on the bridge. To further reveal the influence law of the PWB height, Figure 13 shows the peak absolute values of $\Delta C'_{(0.035s)}$, denoted as Max $|\Delta C'_{(0.035s)}|$, during the 'OUT', 'BR', and 'IN' processes at different PWB heights.

At different PWB heights, the time histories of the aerodynamic coefficients of each carriage were consistent during complete running in Tunnels 1 and 2, demonstrating the reliability of Figure 12. The PWB height affected the aerodynamic coefficient fluctuation law in all three processes. At a given PWB height, the ΔC values were higher in the 'OUT' and 'IN' processes than in the 'BR' process. In the 'BR' process, the C_z of the first car monotonously decreased with increasing PWB height (Figure 12(a_1)). The yawing and pitching moments of the head and middle carriages were less sensitive to PWB height in the 'BR' process than in the other processes because both indexes mainly reflect the difference in longitudinal pressure distribution on the carriage. In particular, their sensitivities decreased with decreasing longitudinal pressure difference (see the last paragraph in Section 5.2). In contrast, the yawing moment of the tail carriage was influenced by PWB height (Figure 12(d_3)), possibly because the unsteady wake structure was susceptible to PWB height (Bell et al., 2016).

At the same PWB height, the $\Delta C'_{(0.035s)}$ values of each carriage presented towering peaks in the 'OUT' and 'IN' processes but relatively smooth fluctuations in the 'BR' process (Figure 12). Accordingly, Max $|\Delta C'_{(0.035s)}|$ was considerably lower in the 'BR' process than in the 'OUT' and 'IN' processes (Figure 13). The 'OUT' and 'IN' processes are the controlling links of the PWB design of TBTI.

In all three processes, Max $|\Delta C'_{(0.035s)}|$ trended downward with increasing PWB height. The occasional abnormal phenomenon in the middle (Figure 13(a_0, c_2, and d_2)) and tail (Figure 13(b_3)) carriages during the 'IN' process was possibly induced by the jet flow effect, which increases with PWB height. Max $|\Delta C'_{(0.035s)}|$ was less sensitive to PWB height in the 'BR' process than in the 'OUT' and 'IN' processes (as evidenced by the amplitude reduction of Max $|\Delta C'_{(0.035s)}|$ when H increased from 2.5–4.0 m). Taking the head carriage as an example; the sensitivities of Max $|\Delta C_z{}'_{(0.035s)}|$ and Max $|\Delta C_{my}{}'_{(0.035s)}|$ were 3.0 and 2.1 times higher, respectively, in the 'IN' process than in the 'BR' process (Figure 13(a_1 and d_1)); similarly, the sensitivities of Max $|\Delta C_y{}'_{(0.035s)}|$ and Max $|\Delta C_{mz}{}'_{(0.035s)}|$ were 2.0 and 3.8 times higher, respectively, in the 'OUT' process than in the 'BR' process (Figure 13(b_1 and e_1)).

Adopting the same design parameters along the full-length PWB on the TBTI is clearly unreasonable. The PWB parameters in the BS ($H = 3.0$ m, $\alpha = 30\%$) are assumed to meet the windproof performance demands of that process. To achieve the equivalent windproof performance in the TBS, the PWB must be 4 m high (33% higher than its present height) (Figure 13(a_1, a_2, b_1, b_3, c_1, c_2, d_3, e_1 and e_2)). Taking the head carriage as an example, the Max $|\Delta C_z{}'_{(0.035s)}|$ values at $H = 3.0$ m were 0.11 and 0.28 in the 'BR' and 'IN' processes, respectively. To reduce Max $|\Delta C_z{}'_{(0.035s)}|$ to the value nearest 0.11 (i.e. 0.14), H of the 'IN' process must be increased to 4 m (Figure 13(a_1)). Meanwhile, the Max $|\Delta C_{mx}{}'_{(0.035s)}|$ values at $H = 3.0$ m were 0.018 and 0.04 in the 'BR' and 'IN' processes, respectively, so H of the 'IN' process must reach 4 m to reduce Max $|\Delta C_{mx}{}'_{(0.035s)}|$ to the

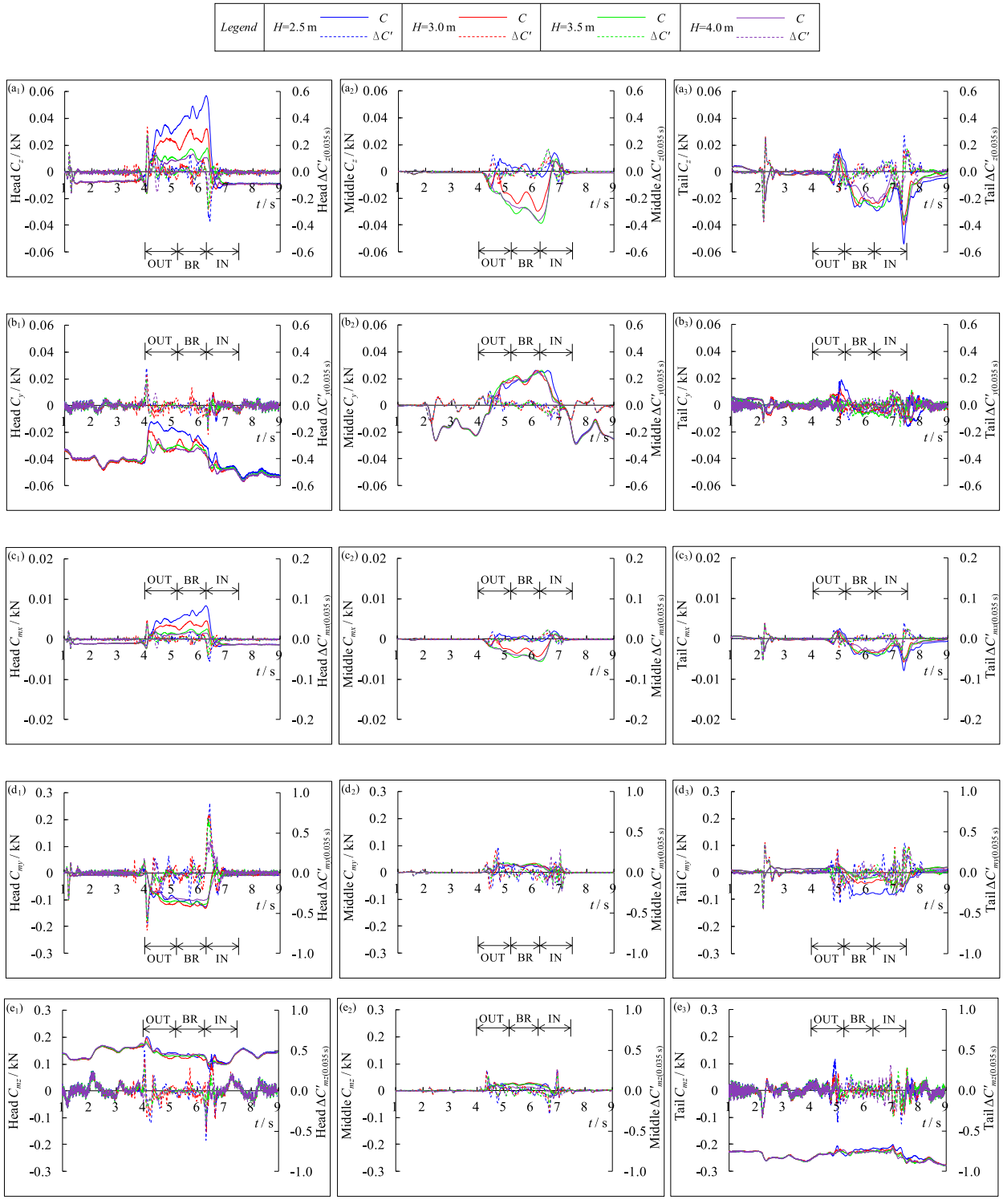

Figure 12. Time-history of aerodynamic coefficients and corresponding change rate of each carriage at different PWB heights: (a) side force, (b) lift force, (c) rolling moment, (d) yawing moment and (e) pitching moment (V_t = 250 km/h; V_w = 25 m/s; α = 30%).

nearest 0.018 (i.e. 0.02) (Figure 13(c_1)). Finally, the Max $|\Delta C_{mz}{}'_{(0.035s)}|$ values at H = 3.0 m were 0.29 and 0.41 in the 'BR' and 'OUT' processes, respectively. To reduce the Max $|\Delta C_{mz}{}'_{(0.035s)}|$ to less than 0.29 (i.e. 0.22) in the 'OUT' process, H must again be increased to 4 m (Figure 13(e_1)).

6.2. Effect of porosity

To investigate the influence law of PWB porosity, Figure 14 shows the variations of the aerodynamic coefficients (solid lines) of the train running on TBT1 and their corresponding change rates (dashed lines) for different PWB

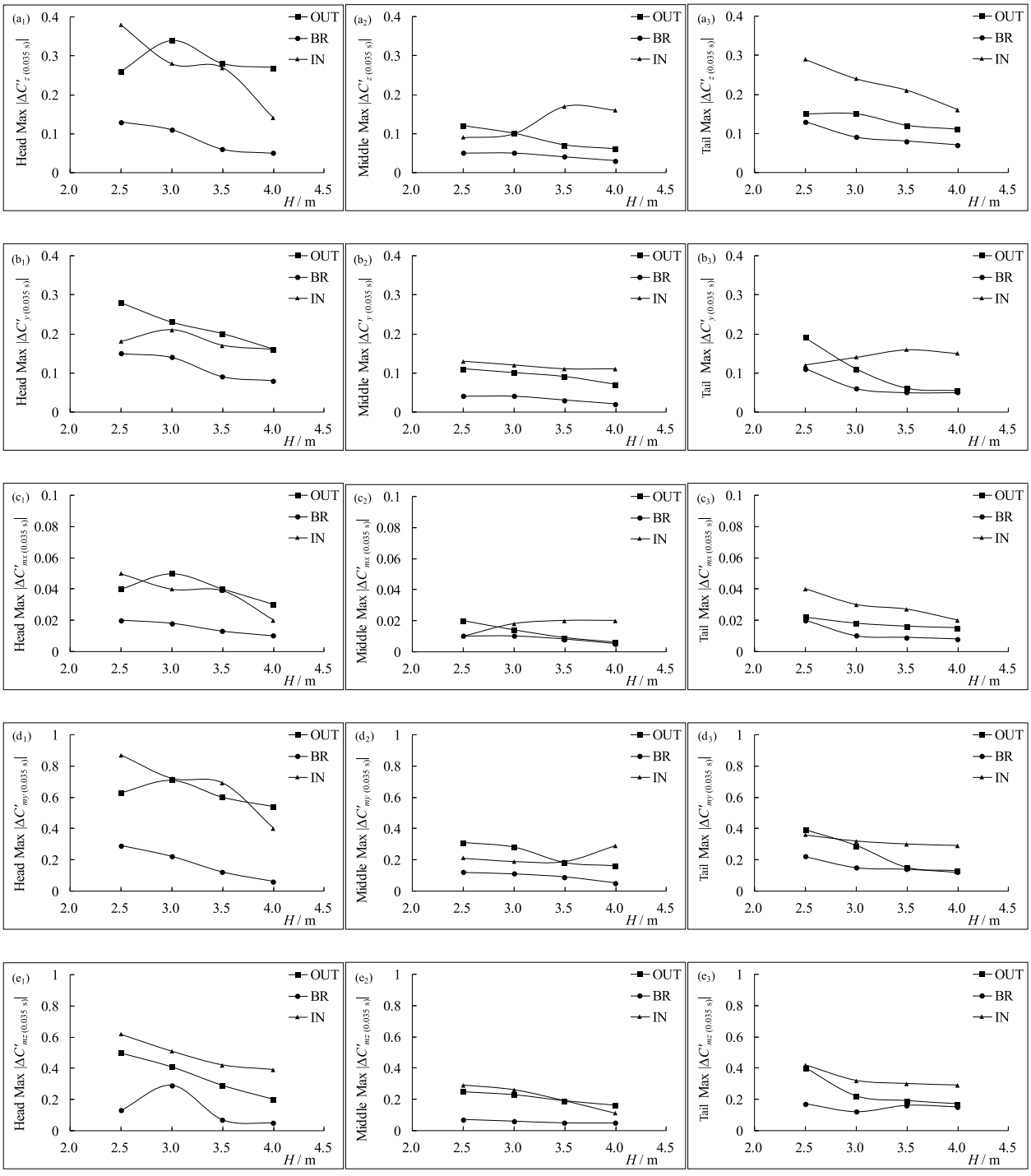

Figure 13. Peak values of the aerodynamic coefficient change rates of each carriage in the 'OUT,' 'BR' and 'IN' processes at different PWB heights ($V_t = 250$ km/h; $V_w = 25$ m/s; $\alpha = 30\%$).

porosities ($\alpha = 20\%, 30\%, 40\%$; $H = 3.0$ m), and Figure 15 shows the peak absolute $\Delta C'_{(0.035s)}$ values of each carriage in the 'OUT', 'BR', and 'IN' processes for each porosity. The findings obtained from these figures are described below.

The α of the PWB affected the aerodynamic coefficient fluctuation law in all three processes. In the 'BR' process, C_z and C_y and C_{mx} monotonously increased with PWB porosity (Figure 14(a–c)). The yawing and pitching moments were minimally sensitive to PWB porosity in the three processes (Figure 14(d and e)).

In the 'OUT' and 'IN' processes, the Max $|\Delta C'_{(0.035s)}|$ of each carriage was approximately positively correlated with PWB porosity (Figure 15(a_1, a_3, b_2, c_1, c_3 and d_1)), because the pressure difference along the length of the train increased with PWB porosity. The porosity

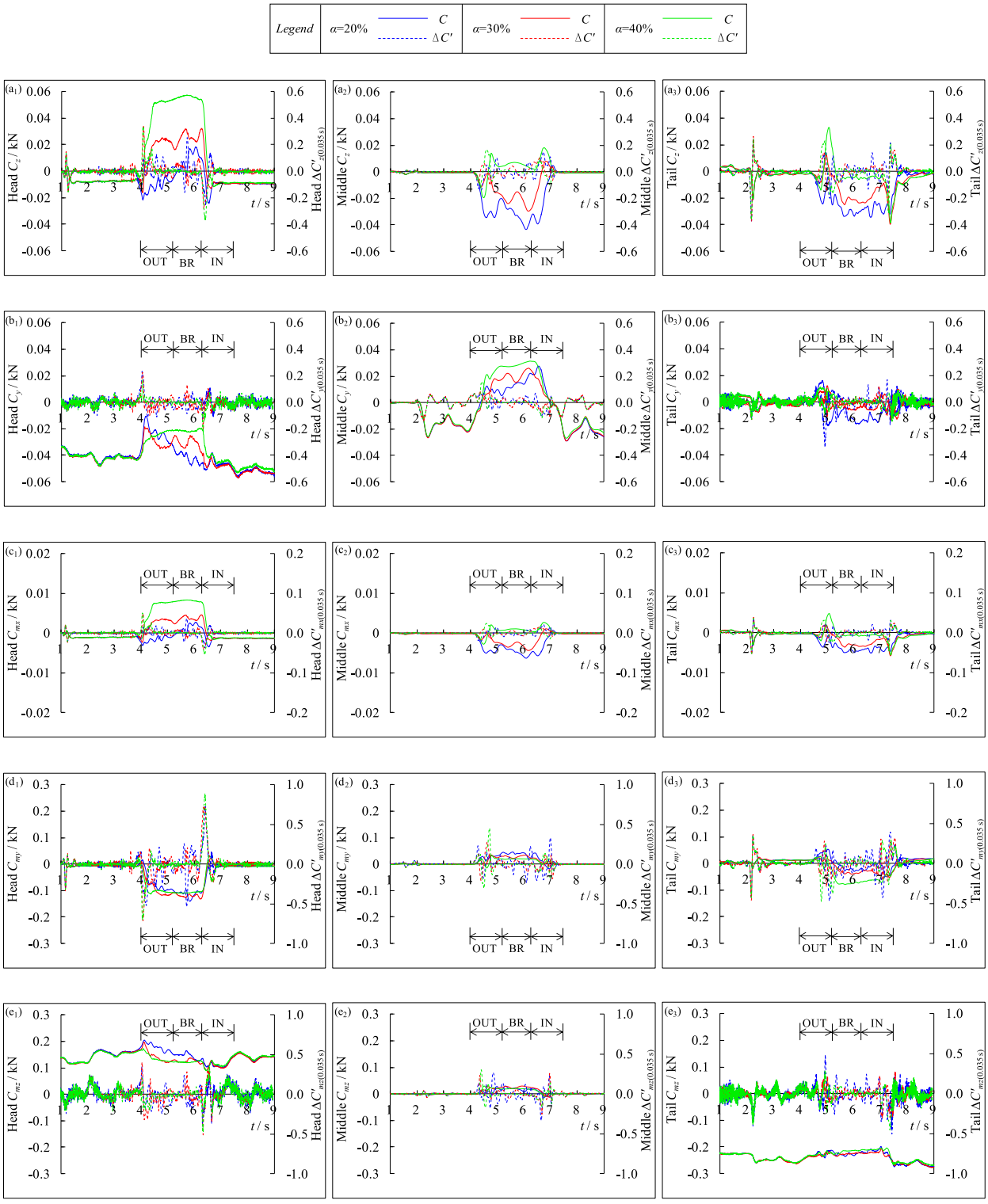

Figure 14. Time-history of the aerodynamic coefficients and corresponding change rate of each carriage at different PWB porosities: (a) side force, (b) lift force, (c) rolling moment, (d) yawing moment and (e) pitching moment (V_t = 250 km/h; V_w = 25 m/s; H = 3.0 m).

oppositely affected the Max $|\Delta C'_{(0.035s)}|$ in the 'BR' and 'OUT/IN' processes. The PWB parameters (H = 3.0 m, α = 30%) were assumed to meet the windproof performance requirements of the 'BR' process. To achieve equivalent windproof performance, the α of the PWB in the TBS must be reduced to 20% (a decrease of 33%) (Figure 15(a_1, b_1, b_2, c_1, c_2 and d_2)). Taking the head carriage as an example, the Max $|\Delta C_z'_{(0.035s)}|$ values at α = 30% were 0.11 and 0.34 in the 'BR' and 'OUT' processes, respectively. To reduce Max $|\Delta C_z'_{(0.035s)}|$ to

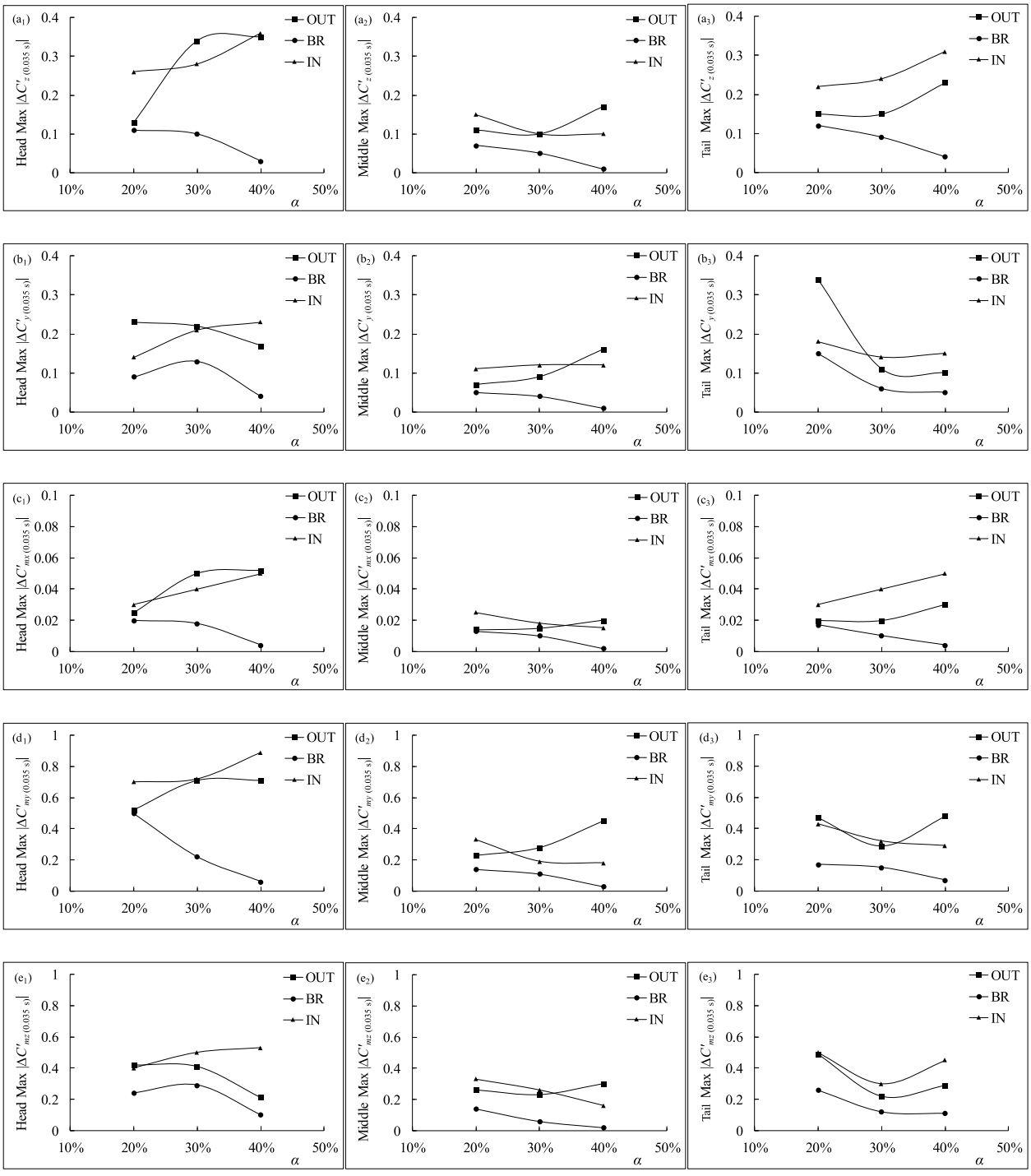

Figure 15. Peak values of the aerodynamic coefficient change rates of each carriage in the 'OUT,' 'BR' and 'IN' processes at different PWB porosities (V_t = 250 km/h; V_w = 25 m/s; H = 3.0 m).

the nearest 0.11 (i.e. 0.13) in the 'OUT' process (Figure 15(a_1)), α must be reduced to 20%. Meanwhile, the Max $|\Delta C_y{}'_{(0.035s)}|$ values atα = 30% were 0.13 and 0.21 in the 'BR' and 'IN' processes, respectively. To reduce Max $|\Delta C_y{}'_{(0.035s)}|$ to the nearest 0.13 (i.e. 0.14) in the 'IN' process (Figure 15(b_1)),αmust be reduced to 20%. Finally, the Max $|\Delta C_{mx}{}'_{(0.035s)}|$ values atα = 30% were 0.018 and 0.05 in the 'BR' and 'OUT' processes, respectively. To reduce Max $|\Delta C_{mx}{}'_{(0.035s)}|$ to the nearest 0.018 (i.e. 0.024) in the 'OUT' process, α must again be reduced to 20% (Figure 15(c_1)).

6.3. Optimization of PWB

Based on the analysis of the previous two subsections, the PWB on TBTI was preliminarily optimized (see

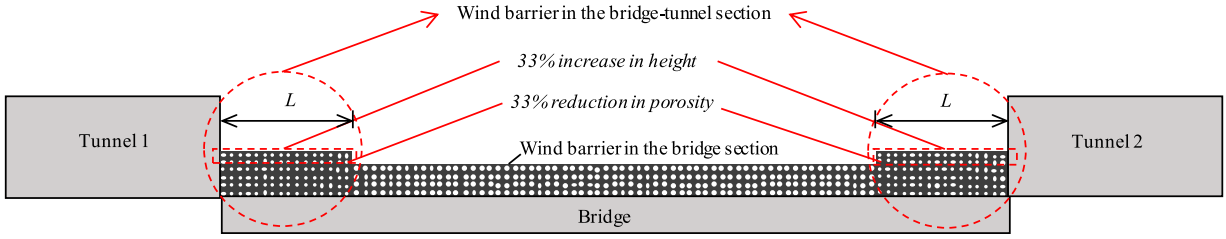

Figure 16. Schematic diagram of PWB optimization on the TBTI.

Figure 16). The parameters of the PWB were selected as $H = 3.0$ m and $\alpha = 30\%$ in the bridge section, and recommended as $H = 4.0$ m and$\alpha = 20\%$ in the TBS. In general, the porosity and height of the PWB in the TBS must be reduced and increased by more than 33%, respectively.

7. Conclusions

This study compares the aerodynamic performance when a train runs on TBTI under crosswind with or without PWBs by building a CFD dynamic model of air–train–PWB. Aiming at the process in the TBS, the influence mechanism of the existence of PWB on the transient aerodynamic effect is revealed from the view point of the flow field. The influences of the height and porosity of the PWB on the transient aerodynamic performance of the HST are discussed. The main conclusions are as follows:

(1) All the aerodynamic coefficients exhibit striking 'pulse' behavior in the process in the TBS under the condition without PWB. The corresponding pulse amplitudes will be reduced by 36–95%, once a PWB is installed.
(2) The pulse amplitudes of the train's aerodynamic loads in the process from bridge to tunnel are 1.03–1.89 times compared with those in the process from tunnel to bridge under the condition without PWB, because the jet flow interferes with the residual longitudinal eddy. The pulse amplitudes in the two processes will be equal when the PWB is installed.
(3) The aerodynamic side force of each carriage is most sensitive to the influence of the existence of PWB, because the PWB weakens the kinetic energy of crosswind flow in the transverse direction.
(4) The TBS is the controlling link of PWB design for TBTI. The sensitivity of the peak values of the aerodynamic coefficient change rates to the influence of PWB height in the TBS are 2.0–3.8 times compared with those in the bridge section.
(5) Adopting the same design parameters along the full-length PWB on the TBTI is unreasonable, e.g. the porosity and the height of the PWB in the TBS need to be reduced and increased by more than 33%, respectively, to achieve equivalent windproof performance.

The results of this study are based on a specific case, and a set of universal design parameters of PWBs in the TBS cannot be obtained yet. Although a preliminary idea for the optimal design is proposed, numerous model and field tests are required to verify its validity. Furthermore, the parameters such as length (L in Figure 16) and the transition form from the bridge–tunnel section to the bridge section also need to be studied and determined. Next step, the authors will do further researches for this issue mentioned above.

Acknowledgments

This work was supported by the National Natural Science Foundation of China (Grant Nos 51978670), The National Science Fund for Distinguished Young Scholars (Grant No. 51925808) and the Project of Science and Technology and Development Plan of China National Railway Group Co., Ltd (Grant Nos. K2019G041 and KYY2020138(20-22)). In addition, the authors would like to thanks Ms. Xinyang Li for her great support for this paper.

Disclosure statement

No potential conflict of interest was reported by the author(s).

Funding

This work was supported by the National Natural Science Foundation of China [grant number 51978670], China National Funds for Distinguished Young Scientists [grant number 51925808]; the Project of Science and Technology and Development Plan of China National Railway Group Co., Ltd [grant number K2019G041], [grant number KYY2020138(20-22)].

ORCID

E. Deng http://orcid.org/0000-0002-0943-9541

References

Avila-Sanchez, S., Lopez-Garcia, O., Cuerva, A., & Meseguer, J. (2016). Characterisation of cross-flow above a railway bridge equipped with solid windbreaks. *Engineering Structures*, *126*, 133–146. https://doi.org/10.1016/j.engstruct.2016.07.035

Bell, J. R., Burton, D., Thompson, M. C., Herbst, A. H., & Sheridan, J. (2016). Dynamics of trailing vortices in the wake of a generic high-speed train. *Journal of Fluids and Structures*, *65*, 238–256. https://doi.org/10.1016/j.jfluidstructs.2016.06.003

Bendjebbas, H., El-Hadj, A. A., & Abbas, M. (2018). Numerical simulation of the effect of wind barrier openings on high-speed wind flow around a heliostat field. *Applied Mathematical Modelling*, *61*, 443–456. https://doi.org/10.1016/j.apm.2018.04.009

Chen, J. W., Gao, G. J., & Zhu, C. L. (2016). Detached-eddy simulation of flow around high-speed train on a bridge under cross winds. *Journal of Central South University*, *23*(10), 2735–2746. https://doi.org/10.1007/ s11771-016-3335-2

Chen, N., Li, Y. L., Wang, B., Su, Y., & Xiang, H. Y. (2015). Effects of wind barrier on the safety of vehicles driven on bridges. *Journal of Wind Engineering and Industrial Aerodynamics*, *143*, 113–127. https://doi.org/10.1016/j.jweia.2015.04.021

Chen, F., Peng, H. R., Ma, X. X., Liang, J. Y., Hao, W., & Pan, X. D. (2019). Examining the safety of trucks under crosswind at bridge-tunnel section: A driving simulator study. *Tunnelling and Underground Space Technology*, *92*, Article 103034. https://doi.org/10.1016/j.tust.2019.103034

Deng, E., Yang, W. C., Deng, L., Zhu, Z. H., He, X. H., & Wang, A. (2020). Time-resolved aerodynamic loads on high-speed trains during running on a tunnel-bridge-tunnel infrastructure under crosswind. *Engineering Applications of Computational Fluid Mechanics*, *14*(1), 202–221. https://doi.org/10.1080/19942060. 2019.1705396

Deng, E., Yang, W. C., He, X. H., Ye, Y. C., Zhu, Z. H., & Wang, A. (2020). Transient aerodynamic performance of high-speed trains passing through an infrastructure consisting of tunnel-bridge-tunnel under crosswind. *Tunnelling and Underground Space Technology*, *102*, Article 103440. https://doi.org/10.1016/j.tust.2020.103440

Deng, E., Yang, W. C., He, X. H., Zhu, Z. H., Wang, H. F., Wang, Y. W., Wang, A., & Zhou, L. (2021). Aerodynamic response of high-speed trains under crosswind in a bridge-tunnel section with or without a wind barrier. *Journal of Wind Engineering and Industrial Aerodynamics*, *210*, Article 104502. https://doi.org/10.1016/j.jweia.2020.104502

Deng, E., Yang, W. C., Lei, M. F., Zhu, Z. H., & Zhang, P. P. (2019). Aerodynamic loads and traffic safety of high-speed trains when passing through two windproof facilities under crosswind: A comparative study. *Engineering Structures*, *188*, 320–339. https://doi.org/10.1016/j.engstruct.2019.01.080

Guo, Z. J., Liu, T. H., Hemida, H., Chen, Z. W., & Liu, H. K. (2020). Numerical simulation of the aerodynamic characteristics of double unit train. *Engineering Applications of Computational Fluid Mechanics*, *14*(1), 910–922. https://doi.org/10.1080/19942060.2020.1784798

He, X. H., Fang, D. X., Li, H., & Shi, K. (2019). Parameter optimization for improved aerodynamic performance of louver-type wind barrier for train-bridge system. *Journal of Central South University*, *26*(1), 229–240. https://doi.org/10.1007/s11771-019-3996-8

He, X. H., Shi, K., Wu, T., & Zou, Y. F. (2016). Aerodynamic performance of a novel wind barrier for train-bridge system. *Wind and Structures*, *23*(3), 171–189. https://doi.org/10.12989/was.2016.23.3.171

He, X. H., Zhou, L., Chen, Z. W., Jing, H. Q., Zou, Y. F., & Wu, T. (2019). Effect of wind barriers on the flow field and aerodynamic forces of a train-bridge system. *Proceedings of the Institution of Mechanical Engineers Part F-Journal of Rail and Rapid Transit*, *233*(3), 283–297. https://doi.org/10.1177/0954409718793220

Kozmar, H., Procino, L., Borsani, A., & Bartoli, G. (2012). Sheltering efficiency of wind barriers on bridges. *Journal of Wind Engineering and Industrial Aerodynamics*, *107–108*, 274–284. https://doi.org/10.1016/j.jweia. 2012.04.027

Kozmar, H., Procino, L., Borsani, A., & Bartoli, G. (2014). Optimizing height and porosity of roadway wind barriers for viaducts and bridges. *Engineering Structures*, *81*, 49–61. https://doi.org/10.1016/j.engstruct.2014. 09.029

Li, W. H., Liu, T. H., Huo, X. S., Chen, Z. W., Guo, Z. J., & Li, L. (2019). Influence of the enlarged portal length on pressure waves in railway tunnels with cross-section expansion. *Journal of Wind Engineering and Industrial Aerodynamics*, *190*, 10–22. https://doi.org/10.1016/j.jweia.2019.03.031

Li, Y. L., Peng, H., Xu, X. Y., & Qiu, J. J. (2017). Wind characteristics at bridge site in a deep-cutting gorge by wind tunnel test. *Journal of Wind Engineering and Industrial Aerodynamics*, *160*, 30–46. https://doi.org/10.1016/j.jweia.2016.11.002

Li, T., Qin, D., Zhang, W. H., & Zhang, J. Y. (2020). Study on the aerodynamic noise characteristics of high-speed pantographs with different strip spacings. *Journal of Wind Engineering and Industrial Aerodynamics*, *202*, Article 104191. https://doi.org/10.1016/j.jweia.2020.104191

Li, T., Yu, M. G., Zhang, J. Y., & Zhang, W. H. (2015). A fast equilibrium state approach to determine interaction between stochastic crosswinds and high-speed trains. *Journal of Wind Engineering and Industrial Aerodynamics*, *143*, 91–104. https://doi.org/10.1016/j.jweia.2015.04.002

Liu, T. H., Chen, Z. W., Zhou, X. S., & Zhang, J. (2018). A CFD analysis of the aerodynamics of a high-speed train passing through a windbreak transition under crosswind. *Engineering Applications of Computational Fluid Mechanics*, *12*(1), 137–151. https://doi.org/10.1080/19942060.2017.1360211

Liu, T. H., Jiang, Z. H., Li, W. H., Guo, Z. J., Chen, X. D., Chen, Z. W., & Krajnovic, S. (2019). Differences in aerodynamic effects when trains with different marshalling forms and lengths enter a tunnel. *Tunnelling and Underground Space Technology*, *84*, 70–81. https://doi.org/10.1016/j.tust.2018.10.016

Mou, B., He, B. J., Zhao, D. X., & Chau, K. W. (2017). Numerical simulation of the effects of building dimensional variation on wind pressure distribution. *Engineering Applications of Computational Fluid Mechanics*, *11*(1), 293–309. https://doi.org/10.1080/19942060.2017.1281845

Niu, J. Q., Zhou, D., & Liang, X. F. (2018). Numerical investigation of the aerodynamic characteristics of high-speed trains of different lengths under crosswind with or without windbreaks. *Engineering Applications of Computational Fluid Mechanics*, *12*(1), 195–215. https://doi.org/10.1080/19942060.2017.1390786

Niu, J. Q., Zhou, D., & Wang, Y. M. (2018). Numerical comparison of aerodynamic performance of stationary and moving

trains with or without windbreak wall under crosswind. *Journal of Wind Engineering and Industrial Aerodynamics*, *182*, 1–15. https://doi.org/10.1016/j.jweia.2018.09.011

Olmos, J. M., & Astiz, M. A. (2018). Non-linear vehicle-bridge-wind interaction model for running safety assessment of high-speed trains over a high-pier viaduct. *Journal of Sound and Vibration*, *419*, 63–89. https://doi.org/10.1016/j.jsv.2017.12.038

Ramezanizadeh, M., Nazari, M. A., Ahmadi, M. H., & Chau, K. W. (2019). Experimental and numerical analysis of a nanofluidic thermosyphon heat exchanger. *Engineering Applications of Computational Fluid Mechanics*, *13*(1), 40–47. https://doi.org/10.1080/19942060.2018.1518272

Rosenfeld, M., Marom, G., & Bitan, A. (2010). Numerical simulation of the airflow across trees in a windbreak. *Boundary-Layer Meteorology*, *135*(1), 89–107. https://doi.org/10.1007/s10546-009-9461-8

Telenta, M., Duhovnik, J., Kosel, F., & Sajn, V. (2014). Numerical and experimental study of the flow through a geometrically accurate porous wind barrier model. *Journal of Wind Engineering and Industrial Aerodynamics*, *124*, 99–108. https://doi.org/10.1016/j.jweia.2013.11.010

Xiang, H. Y., Li, Y. L., Chen, S. R., & Hou, G. Y. (2018). Wind loads of moving vehicle on bridge with solid wind barrier. *Engineering Structures*, *156*, 188–196. https://doi.org/10.1016/j.engstruct.2017.11.009

Xiang, H. Y., Li, Y. L., Hu, Z., & Liao, H. L. (2013). Simulation method of porous wind screen scale model on bridge by wind tunnel tests. *Engineering Mechanics*, *32*(12), 249–256. (In Chinese).

Yang, W. C., Deng, E., Lei, M. F., Zhang, P. P., & Yin, R. S. (2018). Flow structure and aerodynamic behavior evolution during train entering tunnel with entrance in crosswind. *Journal of Wind Engineering and Industrial Aerodynamics*, *175*, 229–243. https://doi.org/10.1016/j.jweia.2018.01.018

Yang, W. C., Deng, E., Lei, M. F., Zhu, Z. H., & Zhang, P. P. (2019). Transient aerodynamic performance of high-speed trains when passing through two windproof facilities under crosswinds: A comparative study. *Engineering Structures*, *188*, 729–744. https://doi.org/10.1016/j.engstruct.2019.03.070

Yang, W. C., Deng, E., Zhu, Z. H., He, X. H., & Wang, Y. W. (2020). Deterioration of dynamic response during high-speed train travelling in tunnel-bridge-tunnel scenario under crosswinds. *Tunnelling and Underground Space Technology*, *106*, Article 103627. https://doi.org/10.1016/j.tust.2020.103627

Yang, W. C., Deng, E., Zhu, Z. H., Lei, M. F., Shi, C. H., & He, H. (2020). Sudden variation effect of aerodynamic loads and safety analysis of running trains when entering tunnel under crosswind. *Applied Sciences-Basel*, *10*(4), Article 1445. https://doi.org/10.3390/app10041445

Yeh, C. P., Tsai, C. H., & Yang, R. J. (2010). An investigation into the sheltering performance of porous windbreaks under various wind directions. *Journal of Wind Engineering and Industrial Aerodynamics*, *98*(10-11), 520–532. https://doi.org/10.1016/j.jweia.2010.04.002

Yu, C. J., Li, Y. L., Zhang, M. J., Zhang, Y., & Zhai, G. H. (2019). Wind characteristics along a bridge catwalk in a deep-cutting gorge from field measurements. *Journal of Wind Engineering and Industrial Aerodynamics*, *186*, 94–104. https://doi.org/10.1016/j.jweia.2018.12.022